



Analysis and Optimization of an Internal Feedback Hydrostatic Turntable Oil Pad Power Consumption Based on Finite Difference Method

Congbin Yang^{1,2} · Shuaihua Shao^{1,2} · Yanhong Cheng^{1,2} · Zhifeng Liu^{1,3} · Yongsheng Zhao^{1,2}

Received: 5 March 2023 / Revised: 20 August 2023 / Accepted: 21 August 2023 / Published online: 25 September 2023
© The Author(s), under exclusive licence to Korean Society for Precision Engineering 2023

Abstract

The hydrostatic turntable is a critical component of numerous CNC machine tools, as it performs a supporting function and enables precise rotary motion. To ensure that high-precision CNC machines can operate under heavy loads, it is imperative to minimize power consumption. The power consumption of a hydrostatic turntable is affected by various factors, such as oil viscosity, initial oil film thickness, and oil pad structure. This study focuses on investigating a hydrostatic turntable with internal feedback. The Reynolds equation of the sector oil pad is solved using the finite difference method to establish the pressure distribution model. Subsequently, the study examines the power consumed by the axial oil pad at different initial oil film thickness, lubricating oil viscosity, and sealing edge width. To minimize power consumption caused by the axial oil pad, this paper employs the genetic algorithm to identify optimal design parameters within specified constraints. Additionally, the load-bearing performance of the optimized axial oil pad is checked to ensure that the load-bearing capacity and stiffness meet the requirements. Finally, the use of simulation software for oil pads in finite element simulation can preliminarily demonstrate the reliability of the proposed method.

Keywords Hydrostatic turntable · Internal feedback · Finite difference method · Genetic algorithm · energy-saving

Abbreviations

A_s	Area of the oil sealing edge and throttle (m^{-2})
A_r	Area of the oil pocket (m^{-2})
b	Width of gap throttle edge (m)
B	Width of oil pad sealing edge (m)
f_r	Friction in the radial direction (N)
f_θ	Friction in the circumferential direction (N)
F_f	Total friction (N)
h	Film thickness (m)

h_0	Initial oil film thickness (m)
h_1	Oil film thickness of upper oil pad (m)
h_2	Oil film thickness of lower oil pad (m)
H	Depth of the oil pocket (m)
i	Numerical counters of the elements of r
j	Numerical counters of the elements of θ
k	Numerical counters of the elements of z
K	Mean stiffness ($N\ m^{-1}$)
l	Length of gap throttle edge (m)
L	Width of oil pad sealing edge (m)
N_f	Total friction power (W)
N_p	Support power (W)
N_t	Total power (W)
\bar{N}_{fr}	Dimensionless friction power in radial direction
p	Pressure (MPa)
p_0	Oil pocket pressure (MPa)
p_s	Inlet pressure (MPa)
p_1	Upper oil pocket pressure (MPa)
p_2	Lower oil pocket pressure (MPa)
Q	Oil supply flow rate ($m^3\ s^{-1}$)
\bar{q}_r	Dimensionless flow rate in radial direction
r	Radial coordinate
R_0	Outside diameters of fan oil pad (m)

✉ Yanhong Cheng
chengyh@bjut.edu.cn

¹ Institute of Advanced Manufacturing and Intelligent Technology, Faculty of Materials and Manufacturing, Beijing University of Technology, Beijing 100124, People's Republic of China

² Beijing Key Laboratory of Advanced Manufacturing Technology, Beijing University of Technology, Beijing 100124, People's Republic of China

³ School of Mechanical and Aerospace Engineering, Key Laboratory of CNC Equipment Reliability, Ministry of Education, Jilin University, Changchun 130012, People's Republic of China

R_1	Inside diameter of fan oil pad (m)
R_{c1}	Oil inlet resistance in upper oil pocket (N s m^{-5})
R_{h1}	Oil outlet resistance in upper oil pocket (N s m^{-5})
R_{c2}	Oil inlet resistance in lower oil pocket (N s m^{-5})
R_{h2}	Oil outlet resistance in lower oil pocket (N s m^{-5})
\bar{U}	Radial velocity (m s^{-1})
\bar{U}_z	Dimensionless damping
V	Circumferential velocity (rad s^{-1})
W	External load on a pair of oil pads (N)
W_0	Oil pad thrust at no load (N)
W_1	Upper oil pad thrust (N)
W_2	Lower oil pad thrust (N)
z	Film thickness coordinate
β_0	Initial throttling ratio
Δh	Oil film thickness variation (m)
θ	Circumferential coordinate
ρ	Density (kg m^{-3})
ω	Rotational angular velocity (rad s^{-1})
ω_{SOR}	SOR weight in successive Over Relaxation method

1 introduction

The hydrostatic turntable plays a crucial role in the performance of many CNC machine tools by providing support and precise rotary motion [1–3]. Therefore, studying the performance of the hydrostatic turntable is essential for enhancing the efficiency of CNC machines. In response to the requirements of high-precision machine tools, internal feedback hydrostatic turntables have been developed. By automatically adjusting the liquid resistance to meet the bearing capacity demands, the internal feedback oil pad can enhance the stiffness of the oil film. The entire turntable possesses a compact structure and stable performance without requiring manual adjustment. Although limited studies have been conducted on internal feedback hydrostatic turntables, some research is available. Some scholars have examined internal feedback hydrostatic bearings and internal feedback hydrostatic guides and have derived a set of corresponding empirical formulas. A torque motor direct-drive internal feedback closed hydrostatic turntable has been designed and implemented, which exhibits greater oil film stiffness and stability compared to a standard hydrostatic turntable. With varying loads, the oil film thickness varies minimally, leading to improved precision.

Typically, hydrostatic support is evaluated by solving the Reynolds equation [4]. The finite difference method is a relatively mature method for solving the Reynolds equation. Ochoa et al. [5] proposed a general form of the Reynolds equation for lubrication applications. Wang et al. [6] modified the Reynolds equation to solve the difficulties of analytically solving second order partial differential equations involving parameters such as pressure, oil film thickness,

oil viscosity, density, and loading surface velocity. Kumar and Liu [7, 8] derived the Reynolds equation for different oil pocket types using the fluid Navier–Stokes equations (N–S equation). Garratt et al. [9–11] also analyzed the Reynolds equation considering the centrifugal force and analyzed the thermal characteristics. These studies proposed many different forms of the Reynolds equation and different numerical solutions of Reynolds equation. They provide the necessary basis for the analysis of hydrostatic support performance.

The optimization of hydrostatic systems has been studied by many scholars recently. Niranjan et al. [12] analyzed the comprehensive effects of recess shape and liquid film thickness on the performance characteristics of hydrostatic guideways, and proposed a recess shape that exhibited superior performance. Zuo et al. [13] researched the impact of various parameters on a self-compensating hydrostatic rotary bearing and obtained the optimal parameters. Christoph [14] improved the bearing performance of a hydrostatic spindle by optimizing the oil film form. Boedo et al. [15] used the genetic algorithm to optimize the shape of radial sliding bearings. Wang et al. [16] used the particle swarm optimization algorithm to optimize the structure of the oil pad, thus reducing the support power. Cai et al. [17] optimized the structure of the oil pad to improve the stiffness of the hydrostatic guide rail. Hang et al. [18] applied the particle swarm optimization method to study the optimization problem of the rectangular oil pad of the air float. Chan et al. [19] applied the multi-objective particle swarm optimization (PSO) method to optimize the load-bearing capacity in the hydrostatic spindle load-bearing model. Cai et al. [20] discussed the optimization scheme for the resistance to overturning of gantry guide rail. Cheng et al. [21] carried out a sensitivity analysis on the structural size parameters of the hydrostatic turntable and combined the particle swarm optimization method to improve the static and dynamic load performance of the turntable. Yu et al. [22, 23] analyzed the influence of the groove structure of a hydrostatic thrust bearing on the comprehensive tribological performance. These studies address a variety of hydrostatic systems, such as hydrostatic bearings, hydrostatic turntables, hydrostatic guideways, hydrostatic rams. From these studies, it is possible to find out the performance changes of these hydrostatic systems, such as bearing capacity, stiffness, flow rate, etc. In addition, many optimization methods were proposed by them, which provided guidance for the subsequent research.

Previous studies aimed at improving the load-carrying performance of hydrostatic turntables [24, 25]. Only a few of the published studies focused on power consumption [26]. Research focused on reducing energy consumption is also a prominent avenue within the realm of future machine tool studies [27–29]. The power consumption of the hydrostatic turntable is considerably lower than that of the conventional mechanical turntable since there is no direct contact between

the hydrostatic turntable and the oil pad. However, even when the load requirements are met, the power consumption of the hydrostatic turntable can still be optimized. In this paper, we employed a torque motor direct-drive internal feedback closed hydrostatic turntable. We simplified the Reynolds equation and established the pressure distribution model using the finite difference method. We analyzed the effects of initial oil film thickness, lubricating oil viscosity, and sealing edge width on the oil supporting power and friction power of the oil pad. Our analysis revealed that viscosity and initial oil film thickness have opposing effects on oil supporting power and friction power. Subsequently, we selected optimal design parameters using the genetic algorithm to minimize the total power of the oil pad. Subsequently, the load-bearing performance of the optimized oil pad was assessed to ensure that the load-bearing capacity meets the required standards. Finally, we performed finite element simulation of the oil pad using simulation software to verify the method's reliability [30, 31].

2 Principle and Calculation

2.1 Model and Principle of Internal Feedback Hydrostatic Turntable

The structure of a torque motor direct-drive internal feedback closed hydrostatic turntable is shown in Fig. 1. It is mainly supported by the hydrostatic bearing of the middle layer. One type of hydrostatic bearing is the internal feedback hydrostatic bearing. According to the oil supply mode, it belongs to constant pressure oil supply, and the throttling form is internal gap throttling. The working principle is shown in Fig. 2. Internal feedback flow chart is shown in Fig. 3. The constant pressure hydraulic oil enters the oil circuit of the axial bearing. Afterwards it is divided into two paths. One way to the upper oil pad, the other way to the lower oil pad. A Δh gap change occurs when the turntable table is subjected to a downward force

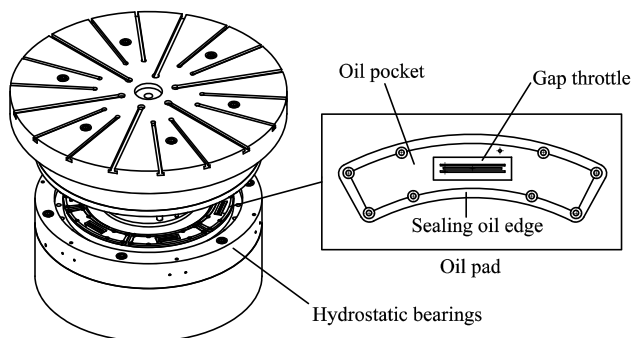


Fig. 1 Internal feedback hydrostatic turntable model

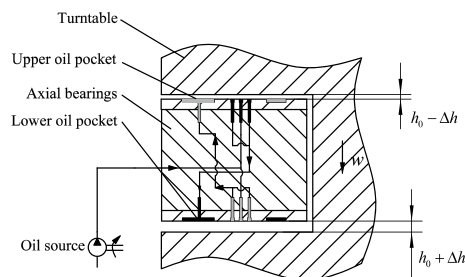


Fig. 2 Working principle of axial oil pad schematic diagram

W . At this moment, on one hand, the decrease in clearance h_1 in the upper oil pocket leads to an increase in oil pocket pressure due to increased oil sealing and increased fluid resistance R_{h1} at the sealing edge. At the same time, the gap throttle located in the lower oil pocket, which controls the upper oil pocket, experiences a decrease in fluid resistance R_{c1} at the throttle edge due to the increase in clearance h_2 , resulting in decreased pressure drop during throttling. As a result, the pressure entering the upper oil pocket increases, creating a feedback effect. Similarly, on the other hand, the increase in clearance h_2 in the lower oil pocket leads to a decrease in oil pocket pressure due to decreased oil sealing and decreased fluid resistance R_{h2} at the sealing edge. The gap throttle located in the upper oil pocket, which controls the lower oil pocket, experiences an increase in fluid resistance R_{c2} at the throttle edge due to the decrease in clearance h_1 , resulting in increased pressure drop during throttling. This leads to a decreased pressure entering the lower oil pocket, also creating a feedback effect. This is how the internal feedback bearing works. Through the combined effect of the upper and lower oil pockets (i.e., a closed-loop hydrostatic bearing structure) and the feedback effect of the gap throttles, the internally self-feedback closed-loop hydrostatic bearing exhibits higher oil film stiffness and stability compared to traditional hydrostatic bearings, with smaller variations in oil film thickness under different loads and better precision retention.

The relationship between oil pressure and fluid resistance is shown in Fig. 4. From the graph, the pressure in the oil pocket can be determined. The pressure in the upper oil pocket can be expressed using the following formula:

$$P_1 = \frac{P_s}{1 + \frac{R_{c1}}{R_{h1}}} = \frac{P_s}{1 + (\beta_0 - 1) \left(\frac{h_1}{h_2}\right)^3} \tag{1}$$

The pressure in the lower oil pocket can be expressed using the following formula:

Fig. 3 Internal feedback flow chart

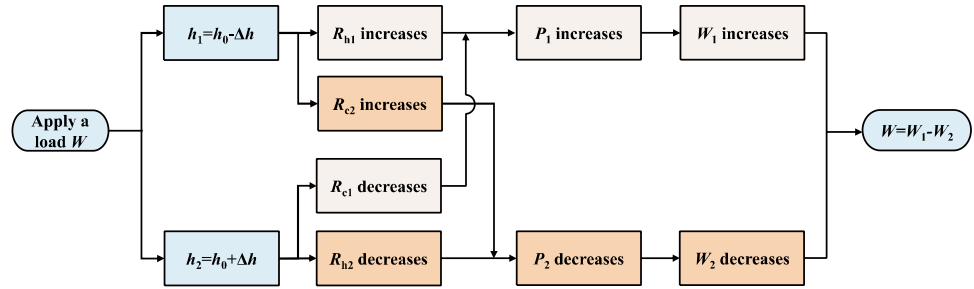
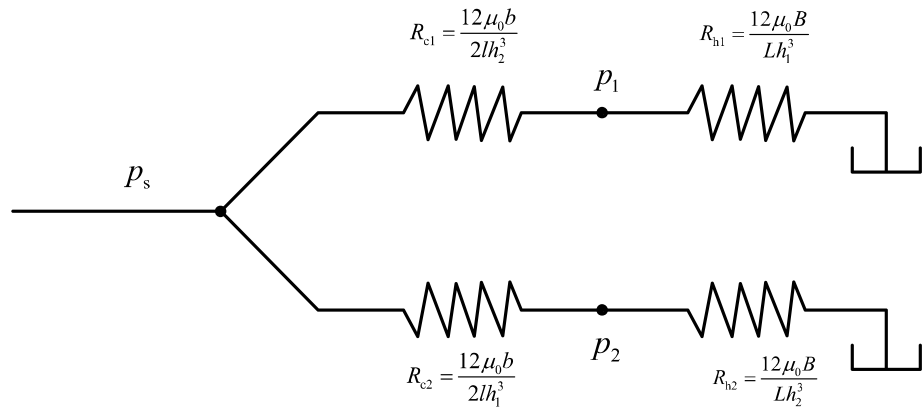


Fig. 4 The relationship between oil pressure and hydraulic resistance



$$P_2 = \frac{P_s}{1 + \frac{R_{c2}}{R_{h2}}} = \frac{P_s}{1 + (\beta_0 - 1) \left(\frac{h_2}{h_1}\right)^3} \tag{2}$$

The support for the internal feedback hydrostatic turntable is a closed support [32, 33]. The table is subjected to a pair of forces of equal magnitude and opposite direction in the no-load condition. Therefore, the load-bearing force of a pair of oil pads is zero when under no load. The table sinks Δh to reach the equilibrium position when the load W is applied. The upper oil pad clearance decreases to $h_1 = h_0 - \Delta h$ while the thrust W_1 increases. The lower oil pad clearance increases to $h_2 = h_0 + \Delta h$, while the thrust W_2 decreases. The difference between the two thrusts is equal to the external load, expressed by the following equation:

$$W = W_1 - W_2 \tag{3}$$

When the displacement of the table is Δh under the action of W . The average stiffness of the opposed oil pad is:

$$K = \frac{W - 0}{\Delta h - 0} \tag{4}$$

2.2 The Reynolds Equation and FDM Solution

The Reynolds equation is a commonly used tool in the analysis of hydrostatic systems, and it describes the pressure

distribution of the viscous oil film in oil pads. While traditional empirical formulas are easy to calculate, they often lack accuracy and cannot effectively describe the pressure distribution of the oil pad. As such, the Reynolds equation is used to solve for the pressure distribution. The Reynolds equation is derived from the simplification of the fluid Navier–Stokes equation in the form of a thin oil film. Since the dimensions in the thickness direction of the thin oil film are much smaller than those in the other two directions, the gradient of the pressure in the thickness direction can be neglected. This simplification results in a binary second-order partial differential equation that is used to describe the pressure distribution inside the oil pad. The sectorial differential Reynolds equation is expressed as follows:

$$\frac{\partial}{\partial r} \left(r \frac{h^3}{\mu} \frac{\partial p}{\partial r} \right) + \frac{\partial}{\partial \theta} \left(\frac{h^3}{\mu} \frac{\partial p}{r \partial \theta} \right) = 6 \frac{\partial}{\partial r} (rUh) + 6 \frac{\partial}{\partial \theta} (Vh) + 12r \frac{\partial h}{\partial t} + \frac{\partial}{\partial r} \left(\frac{h^3 \omega^2 r^2}{\mu} \rho \right) \tag{5}$$

Dimensionless analysis is a common method used in physical research. It can simplify models with various parameters to improve computational effectiveness. The following dimensionless parameters should be defined as follows:

$$\bar{p} = \frac{p}{p_0}, \bar{r} = \frac{r}{R_0}, \bar{z} = \frac{z}{h_0}, \bar{h} = \frac{h}{h_0}, \bar{\mu} = \frac{\mu}{\mu_0}$$

$$\bar{U} = \frac{U}{\frac{h_0^3 \rho_0}{R_0 \mu_0}}, \bar{V} = \frac{V}{\frac{h_0^3 \rho_0}{R_0 \mu_0}}, \bar{U}_z = \frac{h_0^3 \rho_0}{\mu_0 R_0^2}, \bar{p} = \frac{\rho}{\frac{\mu_0^2 R_0^2}{h_0^4 \rho_0}} \quad (6)$$

Dimensionless scaling of the Reynolds equation is as follows:

$$\frac{\partial}{\partial \bar{r}} (\bar{r} \frac{\bar{h}^3}{\bar{\mu}} \frac{\partial \bar{p}}{\partial \bar{r}}) + \frac{\partial}{\partial \theta} (\frac{\bar{h}^3}{\bar{\mu}} \frac{\partial \bar{p}}{\bar{r} \partial \theta}) = 6 \frac{\partial}{\partial \bar{r}} (\bar{r} \bar{U} \bar{h}) + 6 \frac{\partial}{\partial \theta} (\bar{V} \bar{h}) + 12 \bar{r} \bar{U}_z + \frac{\partial}{\partial \bar{r}} (\frac{\bar{h}^3 \bar{V}^2}{\bar{\mu}} \bar{p}) \quad (7)$$

The discretization solution is then performed, as shown in Fig. 5. According to Taylor’s formula, the partial derivative can be expressed as the difference quotient on the neighboring nodes. During the solution process, the pressure is usually discretized into thousands to tens of thousands of microelements, resulting in a very large discretized matrix. The discretization process is as follows:

$$\left(\frac{\partial \bar{p}}{\partial \bar{r}}\right)_{ij} \approx \frac{\bar{p}_{ij} - \bar{p}_{i-1,j}}{\Delta \bar{r}}, \left(\frac{\partial \bar{p}}{\partial \theta}\right)_{ij} \approx \frac{\bar{p}_{ij} - \bar{p}_{i,j-1}}{\Delta \theta}$$

$$\left(\frac{\partial^2 \bar{p}}{\partial \bar{r}^2}\right)_{ij} \approx \frac{\bar{p}_{i+1,j} - 2\bar{p}_{ij} + \bar{p}_{i-1,j}}{(\Delta \bar{r})^2}, \left(\frac{\partial^2 \bar{p}}{\partial \theta^2}\right)_{ij} \approx \frac{\bar{p}_{i,j+1} - 2\bar{p}_{ij} + \bar{p}_{i,j-1}}{(\Delta \theta)^2} \quad (8)$$

where $p_{i,j}$ denotes the pressure value on node (i, j) .

The Gauss–Seidel iteration is a numerical method for solving systems of linear equations. The discretized Reynolds equation is characterized by the fact that the pressure values at all nodes are applied to the same equation. That is, the Gauss–Seidel iteration solves the Reynolds equation with only one iterative equation for all node values. Therefore, the Gauss–Seidel method is often used in conjunction with the finite difference method for the solution of the Reynolds equation. The formula is expressed as follows:

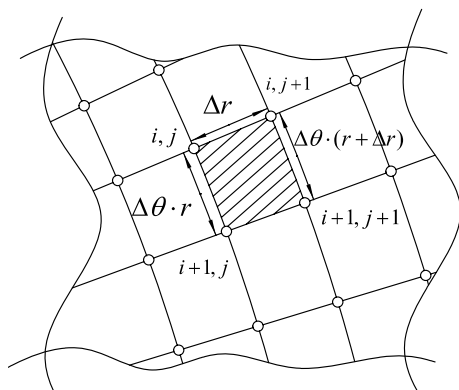


Fig. 5 Discrete nodes of pressure distribution

$$\bar{p}_{ij} = \frac{A(\Delta\theta)^2 + B(\Delta\bar{r})^2 - C\Delta\bar{r}\Delta\theta}{D(\Delta\theta)^2 + E(\Delta\bar{r})^2} \quad (9)$$

where $A = \frac{\bar{r}_i \bar{h}_{ij}^3 \bar{p}_{i+1,j}}{\bar{\mu}_{ij}} + \frac{\bar{r}_{i-1} \bar{h}_{i-1,j}^3 \bar{p}_{i-1,j}}{\bar{\mu}_{i-1,j}}$, $B = \frac{\bar{h}_{ij}^3 \bar{p}_{i,j+1}}{\bar{\mu}_{ij} \bar{r}_i} + \frac{\bar{h}_{i,j-1}^3 \bar{p}_{i,j-1}}{\bar{\mu}_{i,j-1} \bar{r}_i}$

$$C = 6\Delta\theta(\bar{r}_i \bar{h}_{ij} \bar{U}_{ij} - \bar{r}_{i-1} \bar{h}_{i-1,j} \bar{U}_{i-1,j}) + 6\Delta\bar{r}(\bar{h}_{ij} \bar{U}_{ij} - \bar{h}_{i,j-1} \bar{U}_{i-1,j-1}) + 12\bar{r}_i \bar{U}_z \Delta\bar{r} \Delta\theta + \Delta\theta \left(\frac{\bar{h}_{ij}^3 \bar{V}_{ij} \bar{p}_{ij}}{\bar{\mu}} - \frac{\bar{h}_{i-1,j}^3 \bar{V}_{i-1,j} \bar{p}_{i-1,j}}{\bar{\mu}_{i-1}} \right)$$

$$D = \frac{\bar{r}_i \bar{h}_{ij}^3}{\bar{\mu}_{ij}} + \frac{\bar{r}_{i-1} \bar{h}_{i-1,j}^3}{\bar{\mu}_{i-1,j}}, E = \frac{\bar{h}_{ij}^3}{\bar{\mu}_{ij} \bar{r}_i} + \frac{\bar{h}_{i,j-1}^3}{\bar{\mu}_{i,j-1} \bar{r}_i}$$

The boundary conditions of the iterative equation are that the dimensionless pressure inside the oil pocket is all 1, and the dimensionless pressure at the outermost part of the sealing edge is all 0. The boundary conditions can be used to calculate the dimensionless pressure values elsewhere by using Eq. (9). The Successive Over Relaxation method (SOR) is then introduced to accelerate its convergence.

The Successive Over Relaxation method (SOR) is a computational acceleration technique built upon the Gauss–Seidel iteration. It can help the calculation converge faster to meet the required accuracy. Assuming that the iterated calculation value is increased by an increment Δ based on the value of the previous iteration, the formula is expressed as follows:

$$p^{(n+1)} = p^{(n)} + \Delta \quad (10)$$

Multiplying the weight ω_{SOR} before the increment Δ can achieve faster convergence of the iterated calculation value towards the final solution.

$$p_{SOR}^{(n+1)} = p^{(n)} + \omega_{SOR} \cdot \Delta$$

$$p_{SOR}^{(n+1)} = p^{(n)} + \omega_{SOR} \cdot [p^{(n+1)} - p^{(n)}] \quad (11)$$

After rearranging, we obtain the formula for SOR weight adjustment

$$p_{SOR}^{(n+1)} = \omega_{SOR} p^{(n+1)} + (1 - \omega_{SOR}) p^{(n)} \quad (12)$$

where ω_{SOR} is the Over Relaxation Weight, which is generally taken to be between 1 and 2.

The numerical solution process of the Reynolds equation has good convergence, which can be further accelerated by using the Successive Over Relaxation method for iterative computation.

The numerical integral of the pressure across the oil pad area is used to compute the dimensionless bearing capacity of the single sector oil pad:

$$\bar{w} = \sum \frac{1}{4} (\bar{p}_{ij} + \bar{p}_{i+1,j} + \bar{p}_{i,j+1} + \bar{p}_{i+1,j+1}) \cdot \Delta \bar{r} \cdot \Delta \theta \cdot 0.5 \cdot (\bar{r}_{i+1} + \bar{r}_i) \quad (13)$$

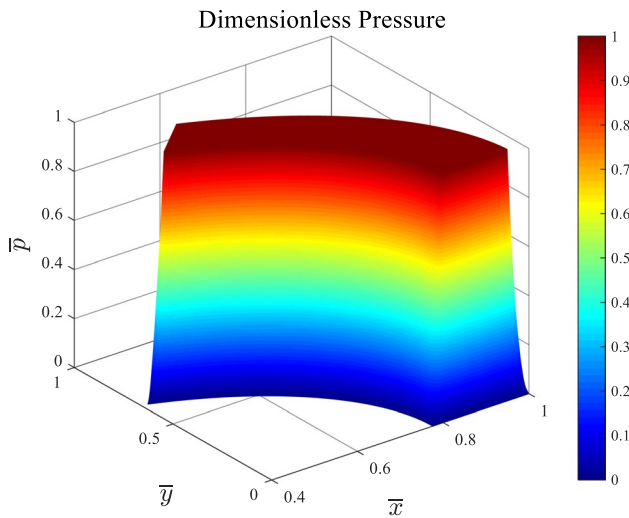


Fig. 6 Sector oil pad pressure distribution model

After further dimensionalization, the bearing capacity of the single sector oil pad is:

$$W = \bar{w} \cdot p_0 \cdot R_0^2 \tag{14}$$

The sector oil pad pressure distribution model can be obtained, as shown in Fig. 6.

2.3 Power Consumption Calculation

Under specific operating conditions, the power consumed by the hydrostatic support comprises two distinct components. The first component involves driving the oil at a certain pressure through the throttle, support gap, pipeline, and other associated devices, and is represented by the output power of the pump or support power. The second component encompasses the power consumption resulting from the friction generated by the relative motion that shears the oil film between the table and the bearing.

(1) Oil supporting power of the oil pump (Support power)

The flow rate should be calculated first, before the support power. The dimensionless flow rate is calculated as the numerical integration of the flow speed over the flow area of the oil film:

$$\begin{cases} \bar{u}_{i,j,k} = \frac{\bar{z}_k^2 - \bar{z}_k}{2\bar{\mu}} \frac{\bar{p}_{i+1,j} - \bar{p}_{i,j}}{\Delta\bar{r}} + \bar{U}_{i,j} \bar{z}_k \\ \bar{q}_r = \sum \left[\frac{1}{4} (\bar{u}_{i,j,k} + \bar{u}_{i,j+1,k} + \bar{u}_{i,j,k+1} + \bar{u}_{i,j+1,k+1}) \cdot \Delta\theta \cdot \bar{r}_i \cdot \frac{1}{2} (\bar{h}_{i,j} + \bar{h}_{i,j+1}) \cdot \Delta\bar{z} \right] \end{cases} \tag{15}$$

where $\bar{r}_i = R_1/R_0$ or $\bar{r}_i = 1$

$$\begin{cases} \bar{v}_{i,j,k} = \frac{\bar{z}_k^2 - \bar{z}_k}{2\bar{\mu}} \frac{\bar{p}_{i+1,j} - \bar{p}_{i,j}}{\Delta\theta \cdot \bar{r}_i} + \bar{V}_{i,j} \bar{z}_k \\ \bar{q}_\theta = \sum \left[\frac{1}{4} (\bar{v}_{i,j,k} + \bar{v}_{i+1,j,k} + \bar{v}_{i,j,k+1} + \bar{v}_{i+1,j,k+1}) \cdot \Delta\bar{r} \cdot \frac{1}{2} (\bar{h}_{i,j} + \bar{h}_{i,j+1}) \cdot \Delta\bar{z} \right] \end{cases} \tag{16}$$

where $\theta=0$ or $\theta=\theta_0$ (θ_0 is the maximum angle of the sector oil pad in radian system).

The total oil discharge flow rate is

$$\bar{q} = \bar{q}_r + \bar{q}_\theta \tag{17}$$

The oil supporting power of the oil pump at the output flow rate Q and the supply pressure p_s is:

$$p_0 = \frac{p_s}{\beta}, Q = \bar{q} \frac{h_0^3 p_0}{\mu_0}, N_p = p_s \cdot Q \tag{18}$$

(2) Friction power

An oil pad must overcome viscous resistance caused by shearing oil film while the turntable rotates. According to the law of Newton inner friction, the friction is expressed as:

$$F_f = \mu A_s \frac{v}{h} + \mu A_r \frac{v}{(h + H)} \tag{19}$$

According to engineering experience, the second term in the above equation is usually not counted when H is greater than the oil pad clearance h more than ten times. However, a quarter of the oil pocket area is included in A_s to roughly estimate the churning loss in the oil pocket, when the viscosity μ is large.

The power consumed to overcome viscous resistance at a certain speed of motion is the friction power. The expression is:

$$N_f = \sum F_f v = \sum \mu A_f \frac{v^2}{h} \tag{20}$$

where $A_f = A_s + \frac{1}{4} A_r$. The equation shows that decreasing the frictional area, using low viscosity oil, and increasing the clearance can all help to reduce the friction force.

Using FDM to solve for friction as the integral of shear stress over the bearing surface:

$$\begin{cases} \bar{f}_r = \sum \frac{1}{4} \left(\begin{matrix} \bar{u}_{i,j,k-1} + \bar{u}_{i+1,j,k-1} + \bar{u}_{i,j+1,k-1} + \bar{u}_{i+1,j+1,k-1} \\ -\bar{u}_{i,j,k} - \bar{u}_{i+1,j,k} - \bar{u}_{i,j+1,k} - \bar{u}_{i+1,j+1,k} \end{matrix} \right) \frac{\bar{\mu} \cdot \Delta \bar{r} \cdot \Delta \theta \cdot \bar{r}_i}{\Delta \bar{z}} \\ \bar{f}_\theta = \sum \frac{1}{4} \left(\begin{matrix} \bar{v}_{i,j,k-1} + \bar{v}_{i+1,j,k-1} + \bar{v}_{i,j+1,k-1} + \bar{v}_{i+1,j+1,k-1} \\ -\bar{v}_{i,j,k} - \bar{v}_{i+1,j,k} - \bar{v}_{i,j+1,k} - \bar{v}_{i+1,j+1,k} \end{matrix} \right) \frac{\bar{\mu} \cdot \Delta \bar{r} \cdot \Delta \theta \cdot \bar{r}_i}{\Delta \bar{z}} \\ f_r = \bar{f}_r h_0 \rho_0 R_0, f_\theta = \bar{f}_\theta h_0 \rho_0 R_0, F_f = \sqrt{f_r^2 + f_\theta^2} \end{cases} \quad (21)$$

The expression for the friction power using FDM is as follows

$$\begin{cases} \bar{N}_{f_r} = \sum \frac{1}{4} \left(\begin{matrix} \bar{u}_{i,j,k-1} + \bar{u}_{i+1,j,k-1} + \bar{u}_{i,j+1,k-1} + \bar{u}_{i+1,j+1,k-1} \\ -\bar{u}_{i,j,k} - \bar{u}_{i+1,j,k} - \bar{u}_{i,j+1,k} - \bar{u}_{i+1,j+1,k} \end{matrix} \right) \frac{\bar{U}_{ij} \bar{\mu} \cdot \Delta \bar{r} \cdot \Delta \theta \cdot \bar{r}_i}{\Delta \bar{z}} \\ \bar{N}_{f_\theta} = \sum \frac{1}{4} \left(\begin{matrix} \bar{v}_{i,j,k-1} + \bar{v}_{i+1,j,k-1} + \bar{v}_{i,j+1,k-1} + \bar{v}_{i+1,j+1,k-1} \\ -\bar{v}_{i,j,k} - \bar{v}_{i+1,j,k} - \bar{v}_{i,j+1,k} - \bar{v}_{i+1,j+1,k} \end{matrix} \right) \frac{\bar{V}_{ij} \bar{\mu} \cdot \Delta \bar{r} \cdot \Delta \theta \cdot \bar{r}_i}{\Delta \bar{z}} \\ N_f = \frac{(\bar{N}_{f_r} + \bar{N}_{f_\theta}) h_0^3 \rho_0^2}{\mu_0} \end{cases} \quad (22)$$

2.4 Genetic Algorithm (GA) Combined with FDM Optimization Process

The genetic algorithm (GA) is a method that simulates the process of biological evolution under natural selection, originally proposed by Darwin [34–36]. By applying this theory, the GA models the problem to be solved as a process of biological evolution. The GA generates the next generation of solutions by using replication, crossover, and mutation operations, sgradually eliminating solutions with low fitness function values and adding solutions with high fitness function values. Due to its good global search capability,

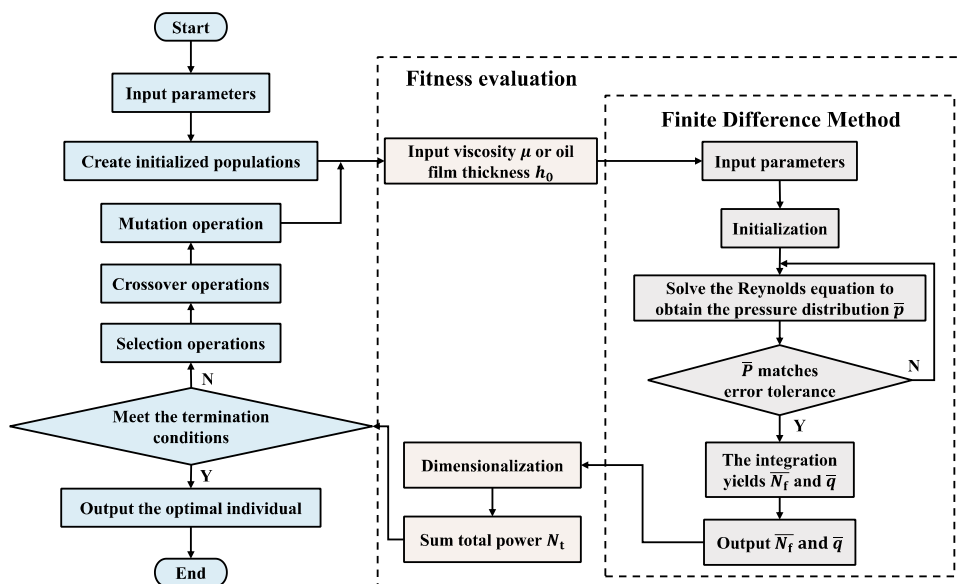
scalability, and the ease of combination with other algorithms, the genetic algorithm has become widely used in optimization problems. In this paper, the GA is utilized to optimize the hydrostatic turntable parameters. The optimization process includes several steps: initialization, fitness evaluation, selection operation, crossover operation, variation operation, and termination condition judgment. The minimum power N_t is output as the optimal solution. The detailed process of optimization using the GA is shown in Fig. 7.

3 Calculation Results and Discussion

3.1 Analysis of the Effect of Viscosity on Power Consumption

Viscosity is a crucial parameter of liquids that directly influences the performance of hydrostatic support and plays a significant role in lubricant selection. The impact of viscosity on the friction force and friction power of the oil pad under different structures is illustrated in Fig. 8, where B represents the width of the oil seal edge. As demonstrated in Fig. 8a, the friction force on the upper surface of the oil pad rises with the viscosity under the same structure. Similarly, Fig. 8b shows that the friction power consumption of the oil pad increases with increasing viscosity under the same structure. This indicates that the friction power consumption generated by the oil pad is mainly caused by the friction force on the upper surface. This phenomenon occurs because higher viscosity means that greater viscous resistance of the oil must be overcome when the table rotates, leading to higher power consumption.

Fig. 7 Sector oil pad power optimization flow chart



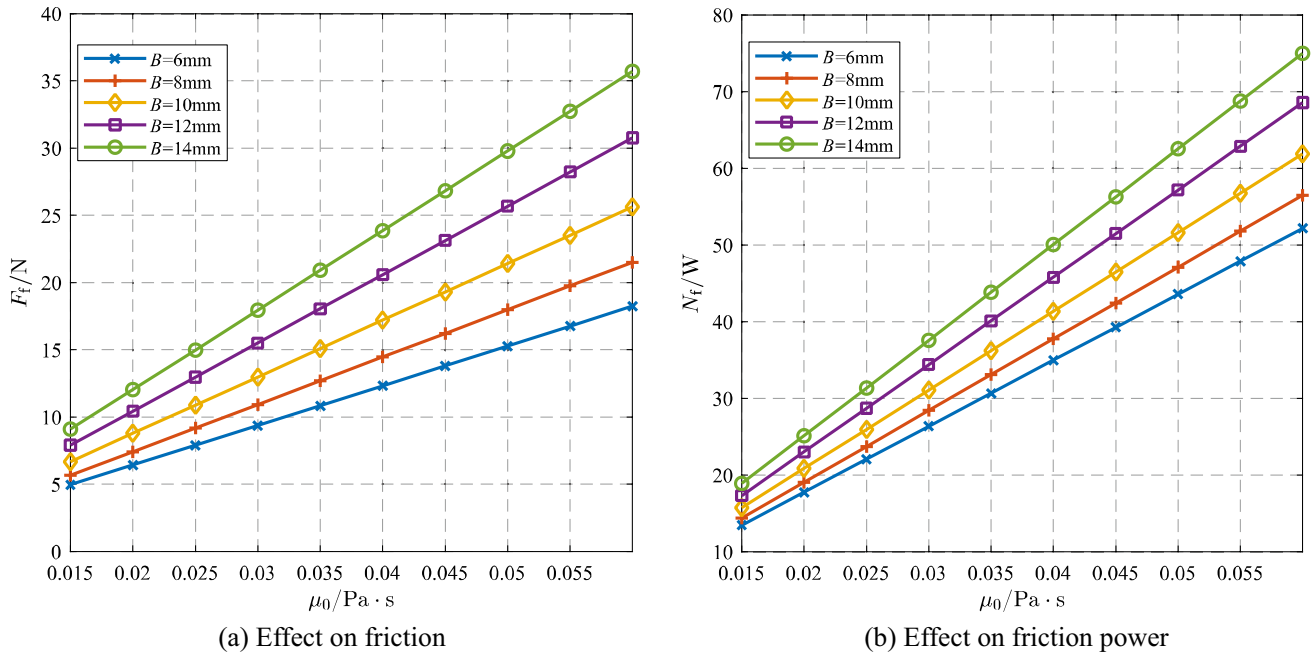


Fig. 8 Effect of viscosity on friction and friction power

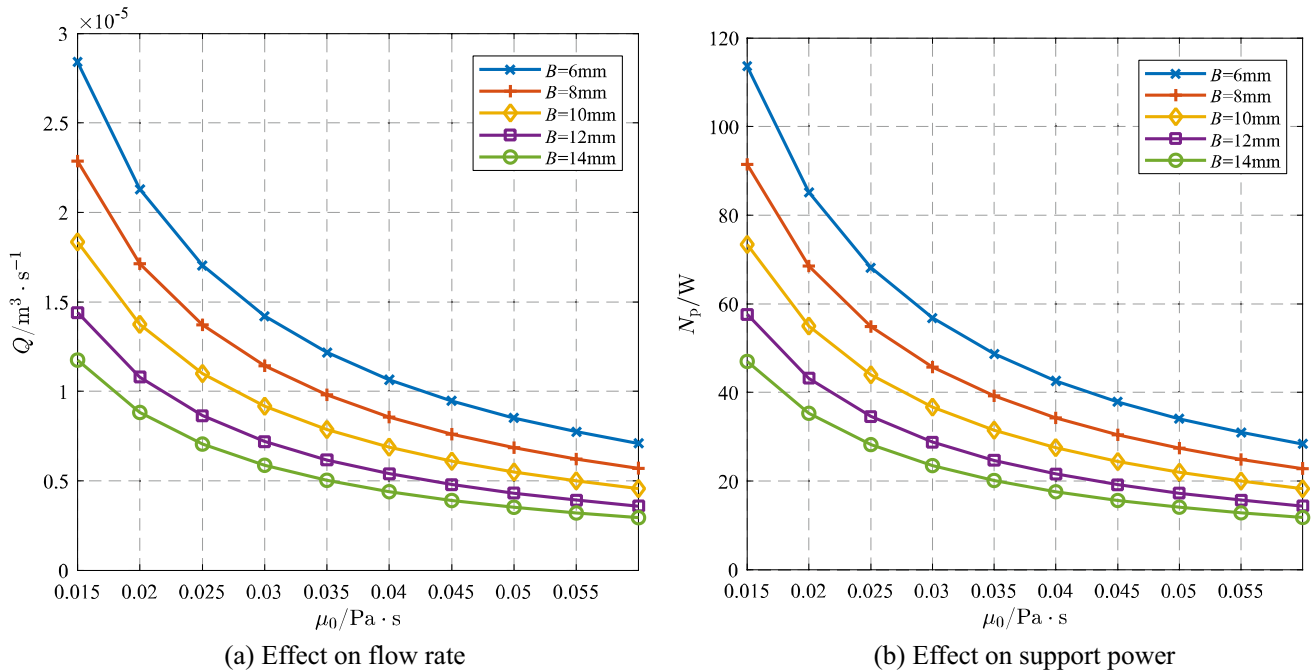


Fig. 9 Effect of viscosity on flow rate and support power

Figure 9 illustrates the impact of viscosity on the oil supply flow and support power of the oil pad under various structures, where B represents the width of the oil seal edge. As demonstrated in Fig. 9a, the oil supply flow rate of the oil pad decreases with an increase in viscosity under the same structure. Similarly, Fig. 9b shows that the support power

consumption of the oil pad decreases with an increase in viscosity under the same structure. These results suggest that the power consumption of the support generated by the oil supply to the oil pad is closely related to the flow rate. This phenomenon can be attributed to the fact that an increase in viscosity leads to an increase in the viscous resistance of the

oil, which in turn causes a decrease in the flow rate of the oil. Consequently, for the same load-carrying performance, less oil needs to be supplied as the viscosity increases. As a result, the oil supply flow rate decreases, leading to a decrease in support power consumption.

3.2 Analysis of the Effect of Initial Thickness on Power Consumption

The initial oil film thickness is a critical parameter that significantly affects the performance of a liquid hydrostatic turntable. This parameter affects both the load-carrying capacity and the power of the oil pad. As shown in Figs. 10 and 11, the friction power and support power of the oil pad exhibit varying trends with the initial oil film thickness, where B represents the width of the oil sealing edge. The initial oil film thickness exhibits an opposite effect on the friction power and support power under the same structure. Specifically, the friction force and friction power decrease as the initial oil film thickness increases. This phenomenon is due to the increase in the gap between the oil pad and the turntable, resulting in an increase in the thickness of the oil film. Based on the law of Newton inner friction, the friction force between the two plates decreases as the gap increases. Conversely, the oil supply flow and support power increase as the initial oil film thickness increases. This result is due to the fact that the increase in oil film thickness decreases the oil discharge resistance, resulting in an increase in flow rate at a constant oil supply pressure.

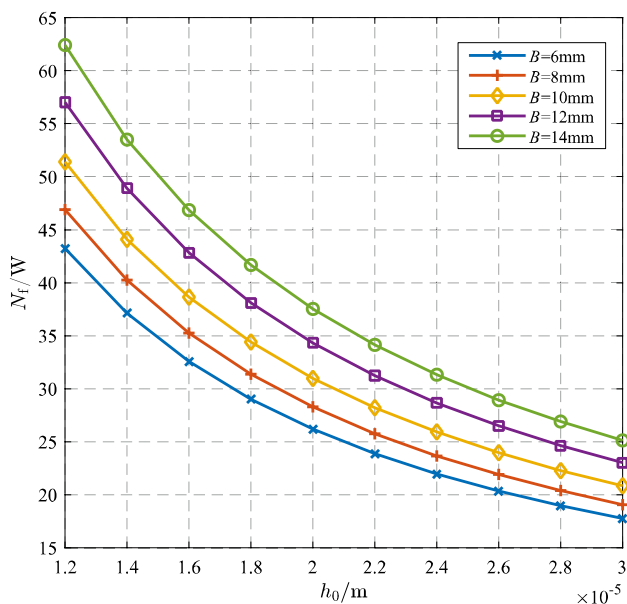


Fig. 10 Effect of initial oil film thickness on friction power

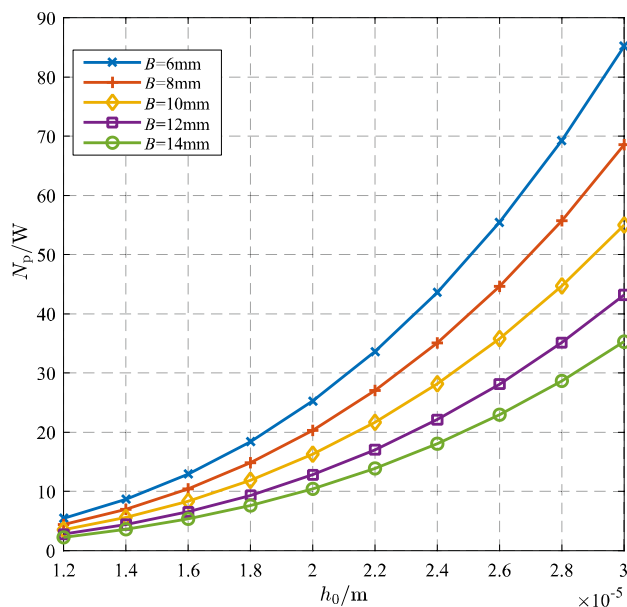


Fig. 11 Effect of initial oil film thickness on support power

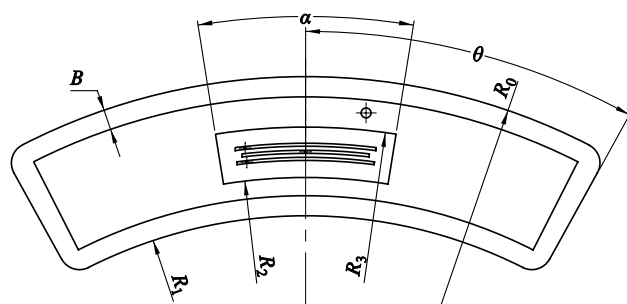


Fig. 12 Diagram of axial oil pad

These four figures, Figs. 8, 9, 10, 11, also show that the width of its oil sealing edge has a minor influence on the power of the oil pad. The widening of the oil sealing edge has opposite effects on friction power and support power. Friction power increases as the oil sealing edge widens due to the increased contact area between the oil pad and the turntable through the oil film. Conversely, support power decreases with the widening of the oil sealing edge. This is because the widening of the oil sealing edge increases the oil outlet resistance of the oil pad, leading to a decrease in the flow rate and support power, under constant oil supply pressure (Fig. 12).

3.3 Genetic Algorithm Based Optimization Solution

Table.1 shows the parameters of a torque motor direct-drive internal feedback closed hydrostatic turntable oil pad, and

Table 1 Values of major parameters

Parameter	Value	Parameter	Value
R_0	308 mm	θ	28°
R_1	239 mm	h_0	0.03 mm
R_2	258 mm	p_s	4 MPa
R_3	283 mm	β_0	2
B	10 mm	μ_0	0.02 pa s
α	9°	W	5000 N

the following is based on this model and optimized according to the process shown in Fig. 7.

(1) Solving for optimal viscosity.

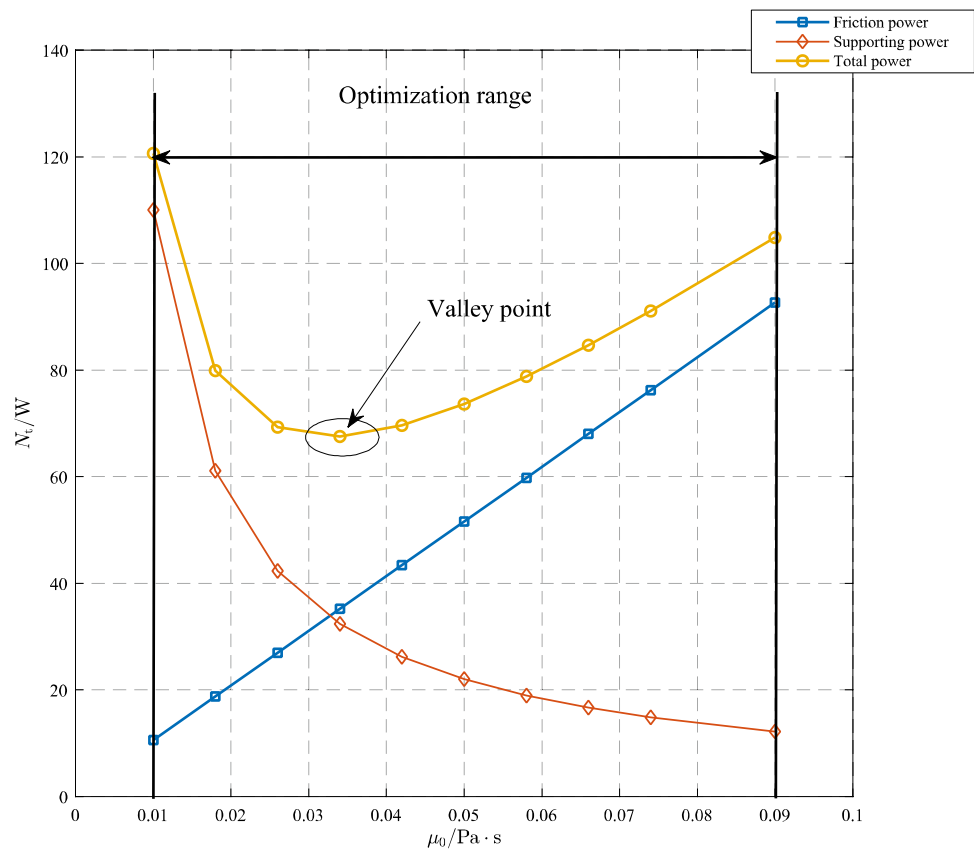
Machine tool hydraulic oil is a commonly utilized lubricant, with different grades established based on technical standards. For instance, 20 and 30 oil are suitable for hydraulic oil in general machine tools, while 10, 20, or 30 oil are appropriate for sliding bearings. Heavy machine tool guides require 40 and 50 oil, while stamping, casting, and other heavy equipment, as well as mining machinery, necessitate 70 and 90 oil. In addition, 20, 30, and 40 oils may be

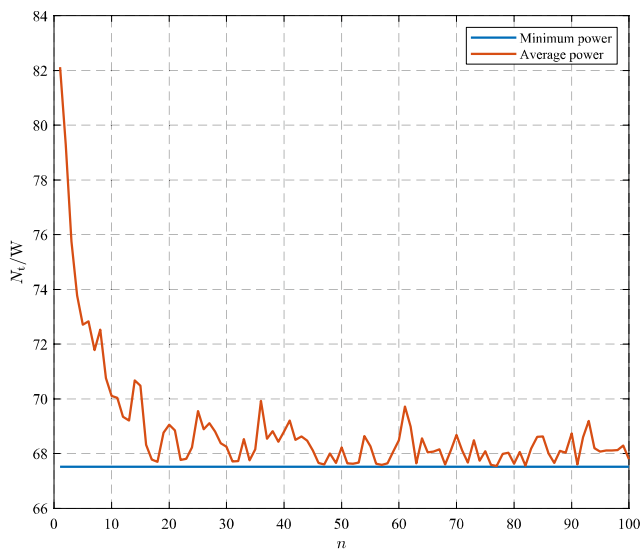
utilized as dual-purpose hydraulic-rail oil on high-precision grinding machines, serving as lubrication for hydraulic and guideway systems in universal grinding machines, bearing grinding machines, thread grinding machines, and gear grinding machines, as well as for the gear and guideway subsets of machine tools. In summary, the optimal machine tool hydraulic fluid power viscosity typically ranges between 0.01 to 0.09 pa s, and the optimization variables are governed within this range, as depicted in Fig. 13.

The initialized population number is $X = 50$ before the optimization begins with viscosity as the variable. The chromosome binary code length is $L_G = 10$ because the viscosity is accurate to 0.0001 ($2^9 < \frac{0.09-0.01}{0.0001} < 2^{10}$). The maximum evolutionary generation $G = 100$, the crossover probability $P_c = 0.8$, and the variation probability $P_m = 0.1$.

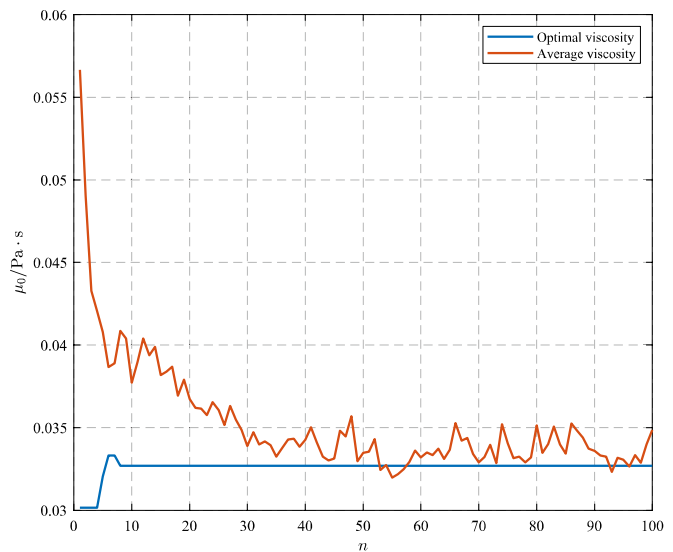
The population individual evolution curve at the end of optimization is shown in Fig. 14. Figure 14 illustrates the optimization process of the genetic algorithm during iteration. The blue line represents the optimal individual, while the red line denotes the average value of all individuals in the population. After 50 iterations, the average value of the population can oscillate around the optimal value. Therefore, the individual with the minimum power consumption can be determined. The optimization result is that the power is minimized when $\mu = 0.0328$ pa s with the value $N_t = 67.53$ W.

Fig. 13 Variation of total power consumption with viscosity





(a) Power of individuals per generation



(b) Position of individuals per generation

Fig. 14 Iterative process of GA solving for optimal viscosity

The oil film gap of the upper oil pad decreases and the oil film gap of the lower oil pad increases when a closed type support is loaded. The resulting axial displacement is $\Delta h = 0.9\mu\text{ m}$ and the rate of change of film thickness is $\epsilon = \frac{\Delta h}{h_0} = \frac{0.9}{30} = 0.03 < 0.2$ when a pair of oil pads are subjected to $W = 5000\text{ N}$ load. Therefore, the load-bearing performance at this viscosity is fully satisfactory.

The difference between the upper and lower oil pad film thicknesses and the initial film thickness is only 3% due to the turntable's very small rate of change in film thickness under a 3t load. There are a total of twelve oil pads in the axial bearing of the hydrostatic turntable. The power consumption of each oil pad does not differ significantly. Therefore, the total power consumption of the axial hydrostatic bearing of the hydrostatic turntable can be approximated as $N_t = 67.52W \times 12 = 810.24W$. In summary, the total power consumption of the axial hydrostatic bearing of the hydrostatic turntable was reduced by 11.55% compared to that before optimization.

(2) Optimal initial oil film thickness solution.

The hydrostatic bearing relies heavily on the presence of a dependable oil film, which is an essential prerequisite for its efficient operation. The failure of the oil film poses a serious safety hazard, which can significantly impair the normal functioning of machine tools. As such, the film's thickness must be carefully regulated to avoid risking oil film failure due to a lack of sufficient thickness. It is worth noting that the oil film thickness in the hydrostatic

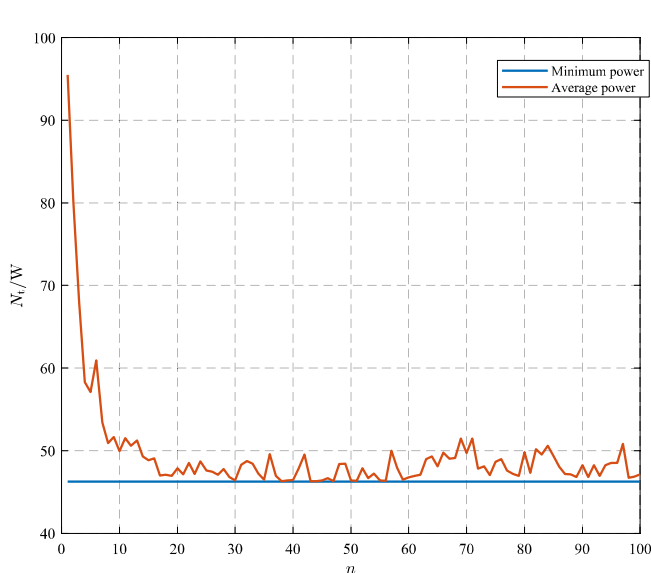
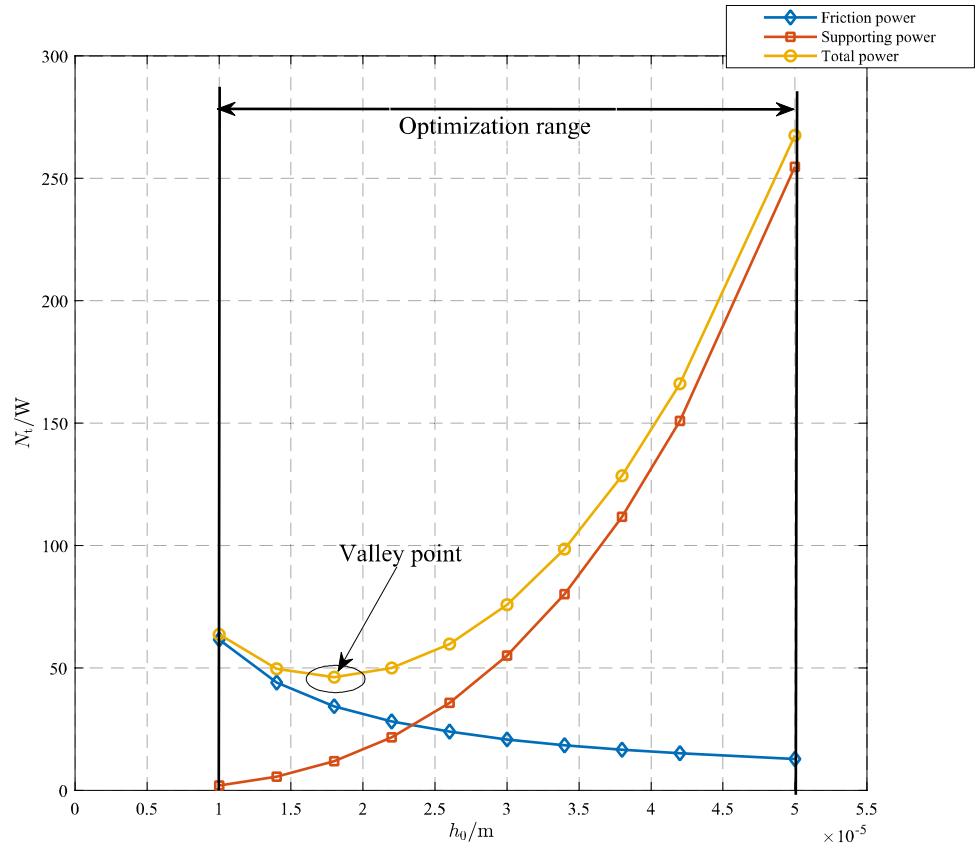
support system's design must be less than the oil boundary layer thickness since the viscous flow of the sealing edge is a necessary condition for maintaining pressure in the oil pocket [37–39]. This ensures the reliability of the Reynolds equation viscous shear stress calculation. In light of the aforementioned variables and potential errors, the initial oil film thickness is established between $10\mu\text{ m}$ to $50\mu\text{ m}$, as depicted in Fig. 15. In addition, the initialized population size is $X = 50$, which is similar to the optimal viscosity solution. The chromosome binary code length is $L_G = 9$. The maximum number of evolutionary generations is $G = 100$. The crossover probability is $P_c = 0.8$ and the variation probability is $P_m = 0.1$.

The population individual evolution curve at the end of optimization is shown in Fig. 15. The optimization result is that the power is minimized when $h_0 = 17.8\mu\text{ m}$ with the value of $N_t = 46.26W \times 12 = 555.12W$. The power is down 39.4% from before optimization. The resulting axial displacement is $\Delta h = 0.5\mu\text{ m}$ under the load of $W = \frac{30000}{6} = 5000\text{ N}$. The rate of change of film thickness is $\epsilon = \frac{\Delta h}{h_0} = \frac{0.5}{17.8} = 0.028 < 0.2$, so the load-bearing performance is also satisfied (Fig. 16).

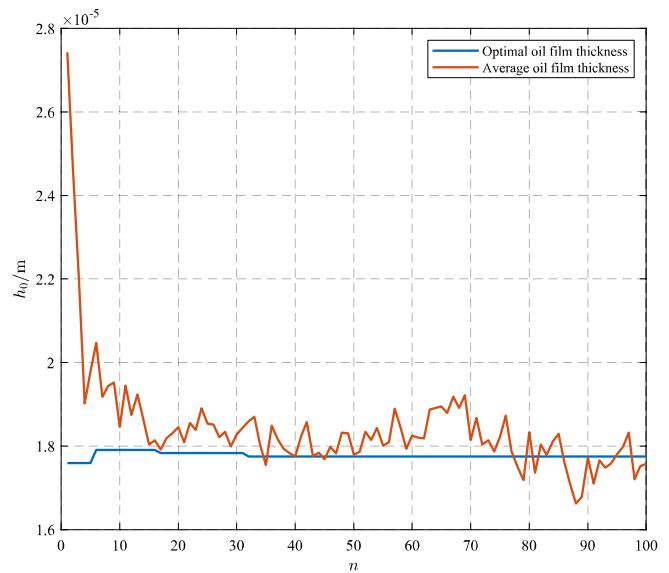
(3) Optimal oil sealing edge width solution.

Figure 17 presents the impact of the oil sealing edge width on the thrust and power of a single oil pad under no-load conditions. As observed from the figure, increasing the size of the oil sealing edge reduces the power consumption, but it also results in a reduction in the thrust of

Fig. 15 Variation of total power consumption with film thickness



(a) Power of individuals per generation



(b) Position of individuals per generation

Fig. 16 Iterative process of GA solving for optimal film thickness

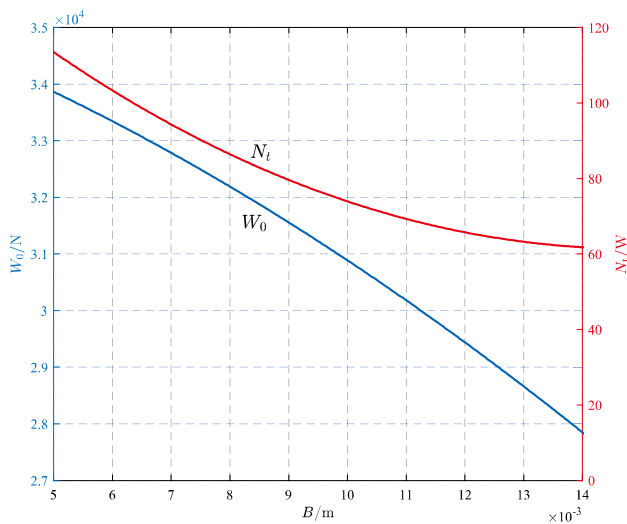


Fig. 17 The relationship between load-bearing performance and oil sealing edge

the oil pad. For closed supports, the thrust of a single oil pad is significantly diminished, resulting in more axial displacement when a load is applied. As a result, the load capacity and stiffness of the entire turntable are reduced. Therefore, it can be inferred that an optimal sealing edge width that minimizes power at a certain pressure does not exist. According to engineering experience and relevant literature [2], for stationary or low-speed rectangular (sector) and circular closed hydrostatic supports, it is generally

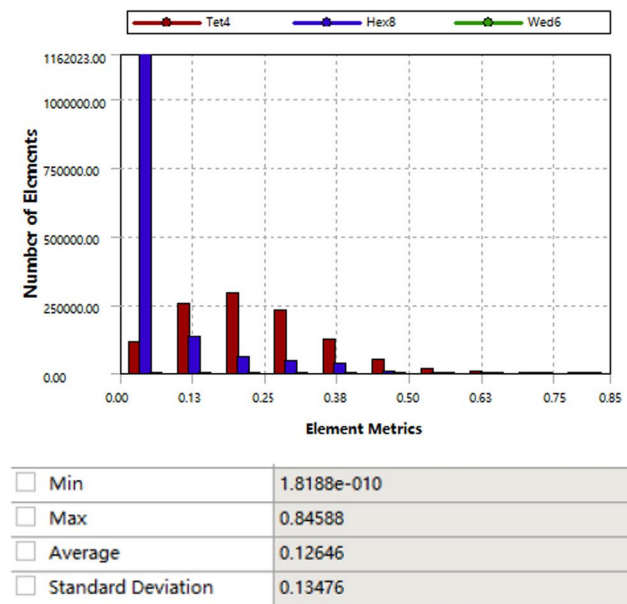
recommended that the ratio of oil sealing edge width to outer diameter should be approximately $\frac{2B}{R_0 - R_1} = 0.3$. The width of the sealing oil edge was calculated to be 10mm, resulting in minimized power, and there is no scope for further optimization.

4 Simulation Verification

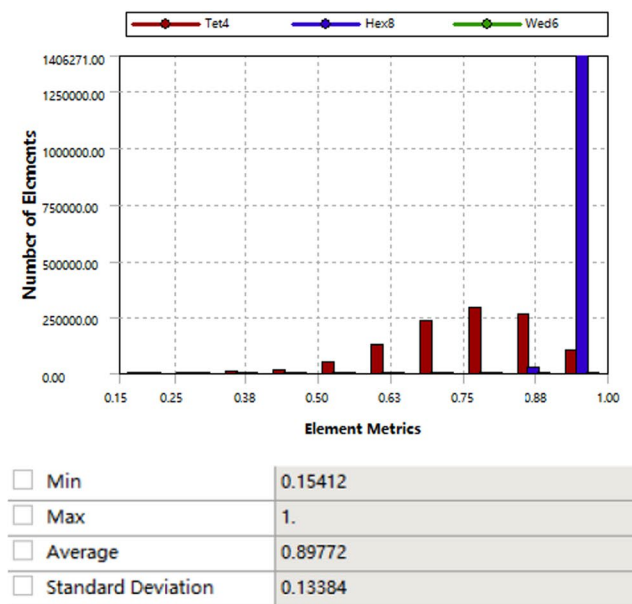
4.1 Calculation Settings

(1) Modeling and meshing

Initially, a three-dimensional oil film model of the bearing was created using Solidworks and then imported into Workbench Mesh for mesh generation. The quality of the mesh directly affects the accuracy of the computation results. In the grid configuration section, the overall size of the grid is set to 0.5 mm. With regards to the oil film region, given its thickness is approximately 0.03 mm and considered as a thin body, the sweeping technique is utilized to construct the grid. Specifically, ten layers of mesh are drawn along the thickness direction, and the mesh is refined in the vicinity of the thin oil film region. The automatic mesh generation method is applied in other areas.



a) Skewness grid quality evaluation



b) Orthogonal Quality grid quality evaluation

Fig. 18 Grid quality check

Upon the accomplishment of grid partitioning, Ansys' Mesh Metric can be employed to assess the quality of the partitioned grid. Skewness, which is one of the primary methods for evaluating mesh quality, can be calculated using two algorithms: Equilateral-Volume-Based Skewness and Normalized Equiangular Skewness. Its numerical value ranges between 0 and 1, with 0 being the most desirable and 1 being the least desirable. Figure 18a illustrates the evaluation of mesh quality using Skewness, which shows that the skewness values of all meshes are below 0.9, with an average value of 0.12. This assures the convergence of the Fluent calculation. Orthogonal Quality is another approach to check the quality of a mesh, with values ranging from 0 to 1, where 0 represents the lowest quality and 1 represents the highest. As shown in Fig. 18b, the minimum orthogonal quality of the mesh is 0.15, and the average orthogonal quality is 0.9. Based on the two aforementioned evaluation criteria, the mesh quality is very high, which provides a solid guarantee for the accuracy of the analysis. After completing the meshing process, it is important to assign names to the inlet, outlet, wall, and interface boundaries for setting up the boundary conditions.

(2) Setting of boundary conditions

(1) *Inlet boundary* The pressure inlet boundary condition is selected at the entrance of the oil pad oil film. According to Eq. (1), with $h_1 = h_2$ in the initial state, the total pressure is set to $p_s/\beta_0 = 2$ MPa.

(2) *Outlet boundary* The outlet is located around the gap of the oil film seal. The outlet boundary is set to the standard atmospheric pressure $P_a = 0$.

(3) *Wall boundary* The upper surface of the oil film is set as "wall_up" and designated as a rotating wall with a rotation speed of 60 rpm, a rotation center at (0, 0, 0), and a rotation axis along (0, 0, 1).

(4) *Defining model* The flow of oil in the oil pad can be approximated as steady-state flow. Therefore, the simulation type is set as "Steady State" and the turbulence model selected under "Fluid Models" is the laminar model.

(5) *Solution control setting* The solution method is set to SIMPLE Scheme, and the other options are set to the default values in Fluent. The initialization method is set as "Hybrid Initialization".

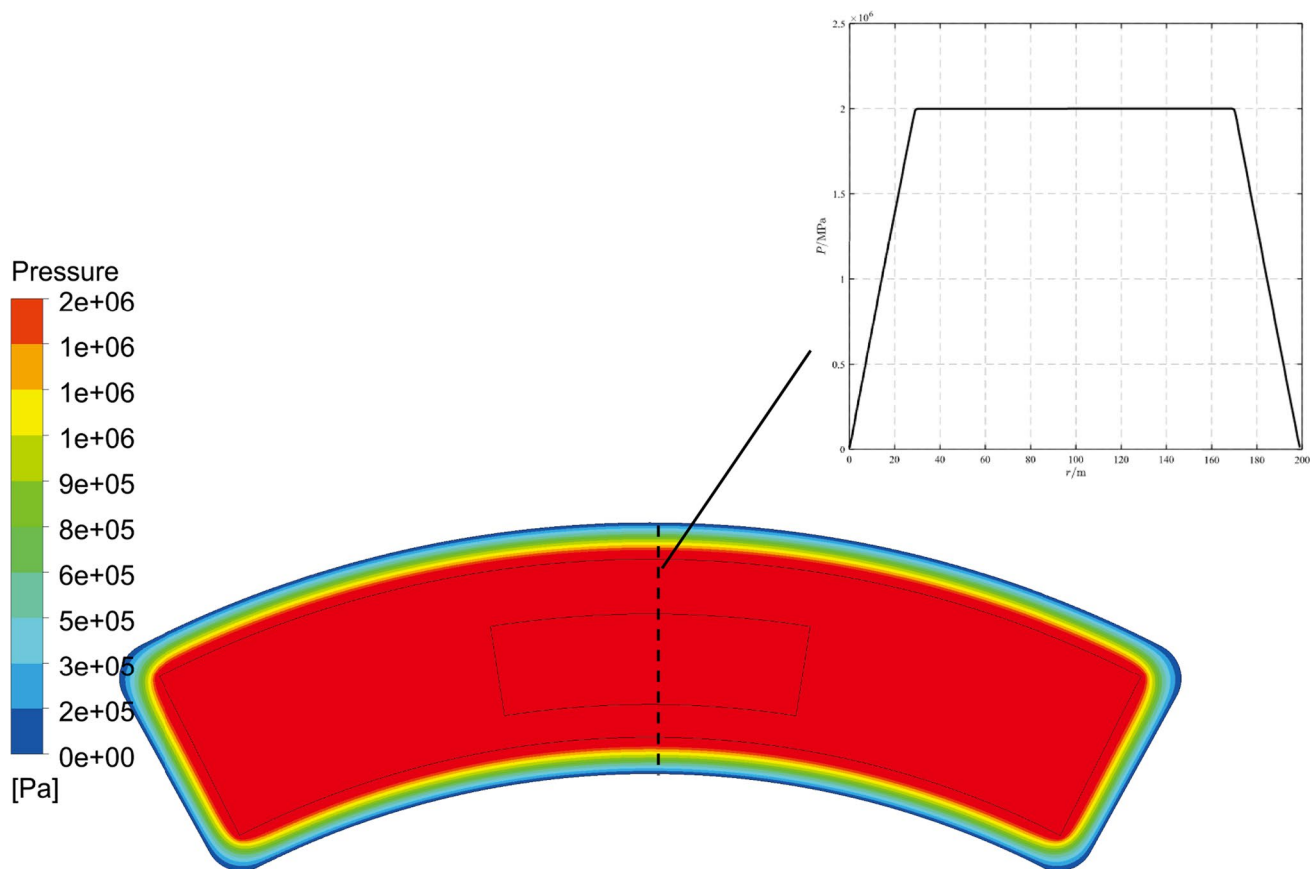


Fig. 19 Pressure cloud map

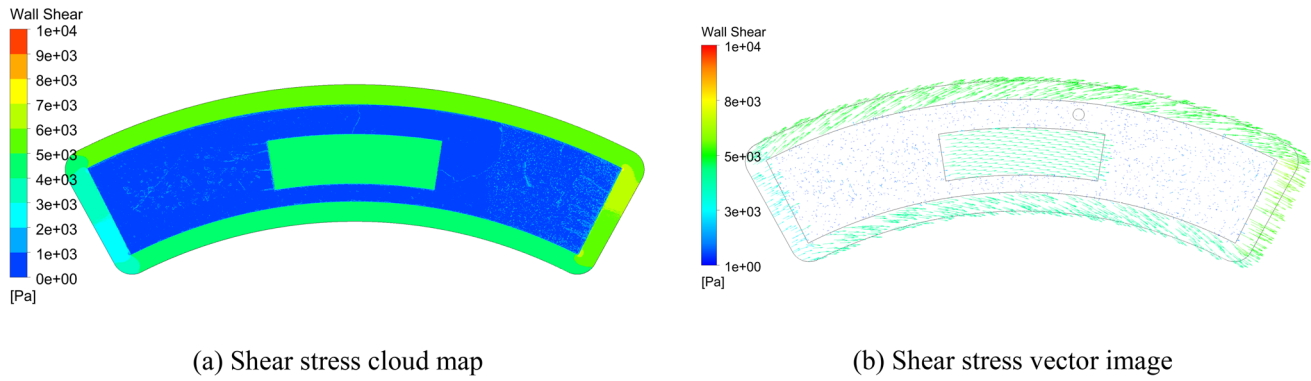


Fig. 20 Shear stress distribution

4.2 Calculation results

The calculated pressure distribution Fig. 19 shows that the pressure in the oil pocket is about 2.14 MPa. The pressure at the raised part of the throttle is equal to the oil pocket pressure. At the oil sealing edge, the pressure is gradually decreasing to 0. This result is consistent with the result calculated by the finite difference method.

Figure 20a and b depict the cloud map of shear stress distribution and the vector diagram of shear stress. The diagram indicates that the friction is relatively high at the raised part of the oil seal edge and the throttle due to the relatively small oil film thickness. In contrast, the oil pocket part exhibits relatively low friction as the depth of the oil pocket is much greater than the oil film thickness. Moreover, the magnitude of the friction force decreases gradually along the direction of rotation of the rotary table. This phenomenon can be attributed to the viscous force that propels the fluid to move with the turntable, thereby causing the oil film to thicken along the rotation direction and reducing the friction force. The direction of the frictional force can be obtained from the arrow direction in Fig. 20b, and the magnitude of the frictional force is reflected by the density of the arrows. Figure 20 a and b together depict the situation of the frictional force acting on the oil pad surface.

4.3 Comparison of results

The main differences between the simulated and theoretical values are: the simulated value is calculated with the finite volume method, while the previous theoretical analysis is calculated with the finite difference method; the controlling equation of the oil film in the simulation is the three-dimensional N-S equation, while the finite difference method is the two-dimensional Reynolds lubrication equation; the previous theoretical analysis simplifies the calculation of the oil pad, while the simulation software

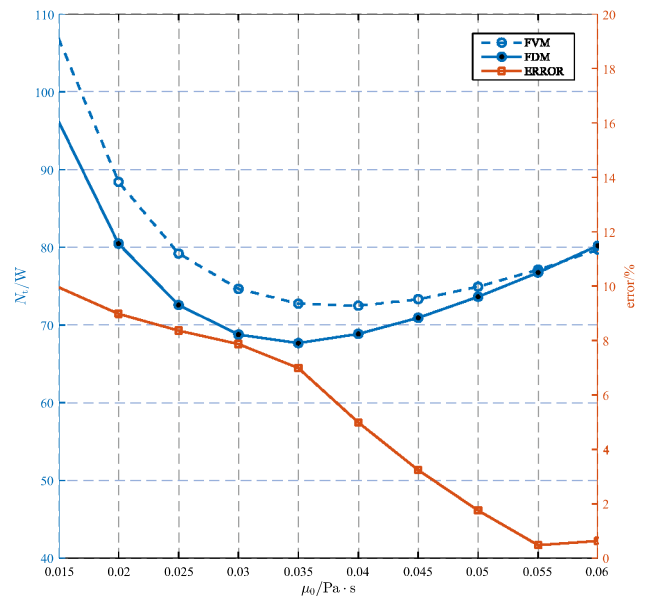


Fig. 21 Comparison of viscosity effects

performs the complete solution. Figures 21, and 22 compare the total power solved by simulation and the finite difference method. Overall, the simulated and theoretical values are in good agreement. The left side of the figure displays the total power consumption, while the vertical axis on the right side indicates the error.

Through a comparison of the theoretical model with the simulation value, it has been observed that there is some degree of error. However, it has also been found that the error range is kept under 10%. This comparison validates the accuracy and reliability of the theoretical model, numerical method, and oil pad optimization results. Therefore, the results obtained from this study can be considered as a reliable reference for the design and optimization of hydrostatic rotary tables.

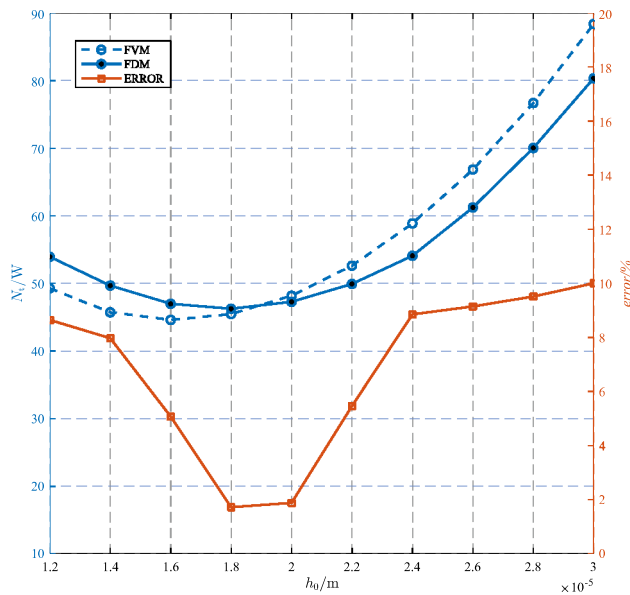


Fig. 22 Comparison of film thickness effects

5 Conclusion

This paper examines the oil pad of an internal feedback hydrostatic turntable, and establishes an oil pad pressure distribution model using the finite difference method. The flow rate, friction force, support power, and friction power were computed, and the effects of viscosity and initial oil film thickness on these quantities were analyzed for different structures. Subsequently, the minimum power consumption was determined through genetic algorithm optimization. Finally, the ANSYS Workbench software was employed to validate the theoretical analysis, demonstrating the method's reliability. Overall, this paper proposes an optimization method for minimizing the power consumption of the oil pad of an internal feedback hydrostatic turntable, leading to the following conclusions:

1. The friction power and support power of the oil pad are inversely correlated with viscosity under the same structural conditions. Specifically, higher viscosity results in lower support power and higher friction power. Thus, selecting an appropriate viscosity can reduce the total power consumption of the pad. The optimization process applied to the model in this study resulted in a total power consumption reduction of 11.6%.
2. The initial film thickness exhibits an opposite effect on the friction and support power of the oil pad under the same structural conditions, which is contrary to the effect of viscosity. Choosing a suitable initial film thick-

ness can similarly reduce the total power consumption of the pad. The optimization process applied to the model in this study led to a total power consumption reduction of 39.4%.

3. The total power consumption of the oil pad decreases as the sealing edge size increases; however, this increase is accompanied by a decline in load-bearing performance. Therefore, there is no optimal width of oil sealing edge that minimizes the total power consumption, and the selection of the appropriate width should be based on the specific circumstances.
4. The results of the ANSYS workbench simulation differ slightly from those of the finite difference method; however, the error is kept under 10%. This provides evidence of the reliability of the finite difference method.

Funding This project is supported by National Natural Science Foundation of China (No. 52175447, No. 51975019), Natural Science Foundation of Beijing Municipality (No. 3232002) and Ministry of Industry and Information Technology's special project for high-quality development of manufacturing industry (No. TC210H039).

Declarations

Competing interest The authors declare no competing financial interests.

References

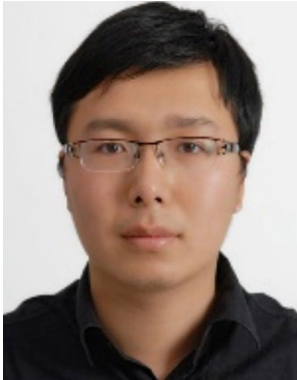
1. Liu, Z. F., Wang, Y. M., Cai, L. G., Zhao, Y. S., Cheng, Q., & Dong, X. M. (2017). A review of hydrostatic bearing system: Researches and applications. *Advances in Mechanical Engineering*, 9(10), 27.
2. Michalec, M., Svoboda, P., Krupka, I., & Hartl, M. (2021). A review of the design and optimization of large-scale hydrostatic bearing systems. *Engineering Science and Technology-an International Journal-Jestech*, 24(4), 936–958.
3. Yu, X., Gao, W., Feng, Y., Shi, G., Li, S., Chen, M., Zhang, R., Wang, J., Jia, W., Jiao, J., & Dai, R. (2023). Research progress of hydrostatic bearing and hydrostatic-hydrodynamic hybrid bearing in high-end computer numerical control machine equipment. *International Journal of Precision Engineering and Manufacturing*, 24(6), 1053–1081.
4. Yin, J., Yu, J., Lou, C., Li, D., Shen, X., & Li, M. (2023). Flow field analysis of lubricating air film in aerostatic restrictor with double U-shaped pressure-equalizing grooves. *International Journal of Precision Engineering and Manufacturing*, 24(2), 145–157.
5. Ochoa, E. D., Otero, J. E., Lopez, A. S., & Tanarro, E. C. (2015). Film thickness predictions for line contact using a new Reynolds–Carreau equation. *Tribology International*, 82, 133–141.
6. Wang, N. Z., Cha, K. C., & Huang, H. C. (2012). Fast convergence of iterative computation for incompressible-fluid Reynolds equation. *Journal of Tribology-Transactions of the Asme*, 134(2), 4.

7. Kumar, V., & Sharma, S. C. (2017). Combined influence of couple stress lubricant, recess geometry and method of compensation on the performance of hydrostatic circular thrust pad bearing. *Proceedings of the Institution of Mechanical Engineers Part J-Journal of Engineering Tribology*, 231(6), 716–733.
8. Liu, Z. F., Wang, Y. M., Cai, L. G., Cheng, Q., & Zhang, H. M. (2016). Design and manufacturing model of customized hydrostatic bearing system based on cloud and big data technology. *International Journal of Advanced Manufacturing Technology*, 84(1–4), 261–273.
9. Garratt, J. E., Hibberd, S., Cliffe, K. A., & Power, H. (2012). Centrifugal inertia effects in high-speed hydrostatic air thrust bearings. *Journal of Engineering Mathematics*, 76(1), 59–80.
10. Su, H., Lu, L. H., Liang, Y. C., Zhang, Q., & Sun, Y. Z. (2014). Thermal analysis of the hydrostatic spindle system by the finite volume element method. *International Journal of Advanced Manufacturing Technology*, 71(9–12), 1949–1959.
11. Liu, Z. F., Zhan, C. P., Cheng, Q., Zhao, Y. S., Li, X. Y., & Wang, Y. D. (2016). Thermal and tilt effects on bearing characteristics of hydrostatic oil pad in rotary table. *Journal of Hydrodynamics*, 28(4), 585–595.
12. Patnana, N., & Nelson, N. R. (2023). Combined effect of recess shape and fluid film thickness on the performance characteristics of hydrostatic guideways. *Proceedings of the Institution of Mechanical Engineers Part C-Journal of Mechanical Engineering Science*, 237(5), 1130–1138.
13. Zuo, X., Li, S., Yin, Z., and Wang, J. (2013). Design and parameter study of a self-compensating hydrostatic rotary bearing. *International Journal of Rotating Machinery*, 2013.
14. Weissbacher, C., Schellnegger, C., John, A., Buchgraber, T., & Pscheidt, W. (2014). Optimization of Journal Bearing Profiles With Respect to Stiffness and Load-Carrying Capacity. *Journal of Tribology-Transactions of the Asme*, 136(3), 6.
15. Boedo, S., & Eshkabilov, S. L. (2003). Optimal shape design of steadily loaded journal bearings using genetic algorithms. *Tribology Transactions*, 46(1), 134–143.
16. Wang, Y. M., Liu, Z. F., Cai, L. G., Cheng, Q., & Dong, X. M. (2018). Optimization of oil pads on a hydrostatic turntable for supporting energy conservation based on particle swarm optimization. *Strojnicki Vestnik-Journal of Mechanical Engineering*, 64(2), 95–104.
17. Cai, L. G., Wang, Y. M., Liu, Z. F., & Cheng, Q. (2015). Carrying capacity analysis and optimizing of hydrostatic slider bearings under inertial force and vibration impact using finite difference method (FDM). *Journal of Vibroengineering*, 17(6), 2781–2794.
18. Chang, S. H., & Jeng, Y. R. (2014). A modified particle swarm optimization algorithm for the design of a double-pad aerostatic bearing with a pocketed orifice-type restrictor. *Journal of Tribology-Transactions of the Asme*, 136(2), 7.
19. Chan, C. W. (2015). Modified particle swarm optimization algorithm for multi-objective optimization design of hybrid journal bearings. *Journal of Tribology-Transactions of the Asme*, 137(2), 7.
20. Wang, Y. M., Liu, Z. F., Cai, L. G., & Cheng, Q. (2018). Modeling and optimization of nonlinear support stiffness of hydrostatic ram under the impact of cutting force. *Industrial Lubrication and Tribology*, 70(2), 316–324.
21. Cheng, Q., Zhan, C. P., Liu, Z. F., Zhao, Y. S., & Gu, P. H. (2015). Sensitivity-based multidisciplinary optimal design of a hydrostatic rotary table with particle swarm optimization. *Strojnicki Vestnik-Journal of Mechanical Engineering*, 61(7–8), 432–447.
22. Yu, X. D., Tang, B. Y., Wang, S. B., Han, Z. L., Li, S. H., Chen, M. M., Zhang, R. M., Wang, J. F., Jiao, J. H., & Jiang, H. (2022). High-speed and heavy-load tribological properties of hydrostatic thrust bearing with double rectangular recess. *International Journal of Hydrogen Energy*, 47(49), 21273–21286.
23. Yu, X. D., Zhang, R. M., Zhou, D. F., Zhao, Y., Chen, M. M., Han, Z. L., Li, S. H., & Jiang, H. (2021). Effects of oil recess structural parameters on comprehensive tribological properties in multi-pad hydrostatic thrust bearing for CNC vertical processing equipment based on low power consumption. *Energy Reports*, 7, 8258–8264.
24. Zhang, Y. Q., Fan, L. G., Li, R., Dai, C. X., & Yu, X. D. (2013). Simulation and experimental analysis of supporting characteristics of multiple oil pad hydrostatic bearing disk. *Journal of Hydrodynamics*, 25(2), 236–241.
25. Hu, H., Rong, Y., Wu, H., & Huang, Y. (2023). Stiffness improvement of aerostatic bearing by separating-pad-based passive compensation. *International Journal of Precision Engineering and Manufacturing*, 24(1), 103–111.
26. Canbulut, F., Sinanoglu, C., & Koc, E. (2009). Experimental analysis of frictional power loss of hydrostatic slipper bearings. *Industrial Lubrication and Tribology*, 61(2–3), 123–131.
27. Li, B., Tian, X., & Zhang, M. (2022). Modeling and multi-objective optimization method of machine tool energy consumption considering tool wear. *International Journal of Precision Engineering and Manufacturing-Green Technology*, 9(1), 127–141.
28. Tesic, S., Cica, D., Borojevic, S., Sredanovic, B., Zeljkovic, M., Kramar, D., & Pusavec, F. (2022). Optimization and prediction of specific energy consumption in ball-end milling of Ti-6Al-4V alloy under MQL and cryogenic cooling/lubrication conditions. *International Journal of Precision Engineering and Manufacturing-Green Technology*, 9(6), 1427–1437.
29. Cai, W., Zhang, Y., Xie, J., Li, L., Jia, S., Hu, S., & Hu, L. (2022). Energy performance evaluation method for machining systems towards energy saving and emission reduction. *International Journal of Precision Engineering and Manufacturing-Green Technology*, 9(2), 633–644.
30. Sun, Y., Wu, Q., Chen, W., Luo, X., & Chen, G. (2021). Influence of unbalanced electromagnetic force and air supply pressure fluctuation in air bearing spindles on machining surface topography. *International Journal of Precision Engineering and Manufacturing*, 22(1), 1–12.
31. Li, K.-Y., Hsieh, P.-C., Wang, J.-J., & Wei, S.-J. (2023). Optimization control method of intelligent cooling and lubrication for a geared spindle. *International Journal of Precision Engineering and Manufacturing*.
32. Wang, Z. W., Liu, Y., & Wang, F. (2017). Rapid calculation method for estimating static and dynamic performances of closed hydrostatic guideways. *Industrial Lubrication and Tribology*, 69(6), 1040–1048.
33. Kang, Y., Chou, H. C., Wang, Y. P., Chen, C. H., & Weng, H. C. (2012). Dynamic behaviors of a circular worktable mounted on closed-type hydrostatic thrust bearing compensated by constant compensations. *Journal of Mechanics*, 29(2), 297–308.
34. Wang, N. Z., & Chang, Y. Z. (2004). Application of the genetic algorithm to the multi-objective optimization of air bearings. *Tribology Letters*, 17(2), 119–128.
35. Katoch, S., Chauhan, S. S., & Kumar, V. (2021). A review on genetic algorithm: Past, present, and future. *Multimedia Tools and Applications*, 80(5), 8091–8126.
36. Ramesh, M., Sundararaman, K. A., Sabareeswaran, M., & Srinivasan, R. (2022). Development of hybrid artificial neural network-particle swarm optimization model and comparison of genetic and particle swarm algorithms for optimization of machining fixture layout. *International Journal of Precision Engineering and Manufacturing*, 23(12), 1411–1430.

37. Lawrence, P. S., & Rao, B. N. (1995). Effect of pressure-gradient on MHD boundary-layer over a flat-plate. *Acta Mechanica*, 113(1–4), 1–7.
38. Naduvinamani, N. B., Hanumagowda, B. N., & Fathima, S. T. (2012). Combined effects of MHD and surface roughness on couple-stress squeeze film lubrication between porous circular stepped plates. *Tribology International*, 56, 19–29.
39. Oh, J. S., Khim, G., Oh, J. S., & Park, C. H. (2012). Precision measurement of rail form error in a closed type hydrostatic guideway. *International Journal of Precision Engineering and Manufacturing*, 13(10), 1853–1859.

Publisher's Note Springer Nature remains neutral with regard to jurisdictional claims in published maps and institutional affiliations.

Springer Nature or its licensor (e.g. a society or other partner) holds exclusive rights to this article under a publishing agreement with the author(s) or other rightsholder(s); author self-archiving of the accepted manuscript version of this article is solely governed by the terms of such publishing agreement and applicable law.



Congbin Yang received Ph.D. degree in School of Mechanical Engineering from Beijing Institute of Technology, Beijing, China, in 2015. Presently, he is a professor in the Institute of Advanced Manufacturing and Intelligent Technology, Beijing University of Technology. His current research interests include dynamics analysis, and Intelligent manufacturing.



Shuaihua Shao is currently a graduate student at the Institute of Advanced Manufacturing and Intelligent Technology, Beijing University of Technology, China. His research interests include the CNC machine tool precision hydrostatic bearing theory and technology.



Yanhong Cheng received Ph.D. degrees from Beijing Jiaotong University, China, in 2020. He is a lecturer in the Institute of Advanced Manufacturing and Intelligent Technology, Beijing University of Technology. His research interests include theory and application of magnetic liquids. He is the corresponding author of the paper.



Zhifeng Liu received Ph.D. degrees from Northeastern University, China, in 2001. Presently, he is a Professor in the Key Laboratory of CNC Equipment Reliability, Ministry of Education, Jilin University. His research interests include machine tool precision design, digital design and manufacture, advanced manufacturing technology, and automation. He was selected as a Chang Jiang Scholars in 2021.



Zhifeng Liu Yongsheng Zhao received Ph.D. degrees from Huazhong University of Science & Technology, China, in 2007. Presently, he is a Professor in the Institute of Advanced Manufacturing and Intelligent Technology, Beijing University of Technology. His research interests include advanced manufacturing technology, and machine tool precision design.